Linking High-Harmonic Generation and Strong-Field Ionization in Bulk Crystals - Supporting Information

Peter Jürgens,[*,†,‡] Sylvianne D.C. Roscam Abbing,[‡] Mark Mero,[†] Clara L. Garcia,[†] Graham G. Brown,[†] Marc J.J. Vrakking,[†] Alexandre Mermillod-Blondin,[†] Peter M. Kraus,[‡,¶] and Anton Husakou[†]

†*Max-Born-Institute for Nonlinear Optics and Short Pulse Spectroscopy, Max-Born-Str. 2A, 12489 Berlin, Germany*

‡*Advanced Research Center for Nanolithography (ARCNL), Science Park 106, 1098 XG Amsterdam, Netherlands*

¶*Department of Physics and Astronomy, and LaserLaB, Vrije Universiteit, De Boelelaan 1105, 1081 HV Amsterdam, Netherlands*

E-mail: juergens@mbi-berlin.de

Experimental Details

Detailed Experimental Methods

All experimental high-harmonic spectra that were analyzed in the main manuscript (Figs. 1-4) were obtained using an integration time of 1 ms of the commercial, fiber-based spectrometer (Avantes AvaSpec-HS1024x58/122TEC). The number of internal averages was set to 10 for every intensity and every orientation angle θ. Taking into account to the 100 kHz

repetition rate and the total acquisition time of 10 ms, a total number of 1000 spectra was analyzed for each datapoint shown in Figs. 1-4. For every intensity of the short-wavelength infrared (SWIR) pump laser pulse the crystal angle was changed in steps of 5° using a computer-controlled rotation state (Thorlabs PRM1Z8). Hence, for every SWIR intensity, the measurement was repeated 72 times to cover a full rotation of the crystalline sample.

Comparing Absorption & Transmission to HHG Yields

Besides analyzing the absorption of the SWIR pump laser pulse and the high-harmonic yields as done in the main manuscript it is also possible to directly compare the orientation-dependent transmission to the harmonic signals. Both methods are compared in Fig. S1. In Fig. S1(a) the absorption is shown together with the normalized yield of the third, fifth and seventh harmonic (curves are offset for visibility). Here, the maxima and the minima of the absorption and the HHG yield align which clearly shows a direct correlation between the two measured quantities. In Fig. S1(b) however, the transmission is shown together with the harmonic yields. Here we observe minima in the transmission when the harmonic signal is maximized and vice versa. This negative correlation maybe favorable in certain conditions. However, we prefer showing the positive correlation between absorption and harmonic signal as - in our opinion - it shows the clearest evidence for the correlation between absorption (photoionization) and the high-harmonic generation process. Note that both approaches are completely valid and capture the same underlying physics.

Angle Calibration

The crystal angles were calibrated by characterizing the anisotropic emission of the third harmonic generation at a SWIR intensity of $2\,\mathrm{TW\,cm^{-2}}$ and compared to the theoretical and experimental results shown in Fig. 2 of Ref.[1] where a four-fold symmetry with maxima along monoatomic nearest-neighbour directions is shown. The results presented by You et al.

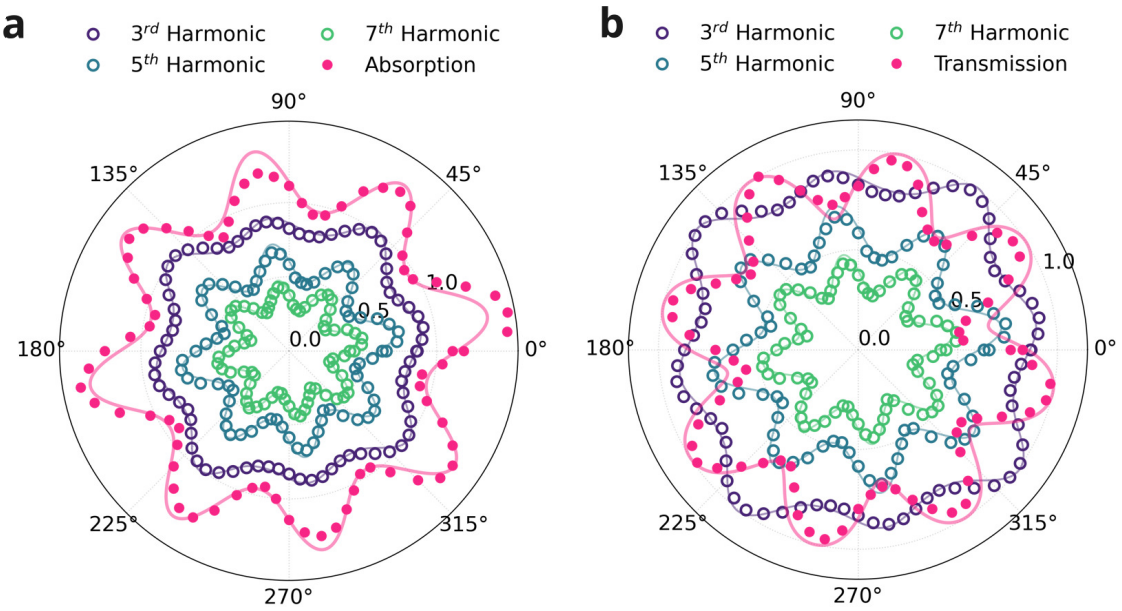

Figure S1: Comparison between showing absorption and transmission of the SWIR pump laser pulses together with the high-harmonic yields. (a). Normalized yields of the observed high-harmonic orders together with the absorption of the fundamental beam as a function of the orientation angle. (b). $\theta-$dependence of the transmission compared to the normalized harmonic yields. Circles show the measured datapoints while solid lines represent numerical fits according to Eq. (1) given in the main manuscript.

based on a perturbative nonlinear susceptibility tensor match our findings in the perturbative range (see Fig. S2) and serve as a calibration for the orientation angle θ.

Extended Analysis of the Orientation-Dependent Measurements

For clearer visibility of the alignment between the extrema observed for the high-harmonic emission and the nonlinear absorption, the experimental results shown in Figs. 2(b), 3(a) and 4(a) are reprinted as Cartesian plots in Figs. S1 (a), (d) and (g) for MgO, Al_2O_3 and LiF, respectively. As in the polar plots in the main text, experimental data points are represented by circles while the numerical fits according to Eq. (1) are represented by the solid lines. Since we base some of the conclusions made in the main manuscript on quantities extracted from the numerical fits applied on the experimental datapoints, we further analyze the agreement between the numerical fits and the experimental data by means of a R^2 analysis.

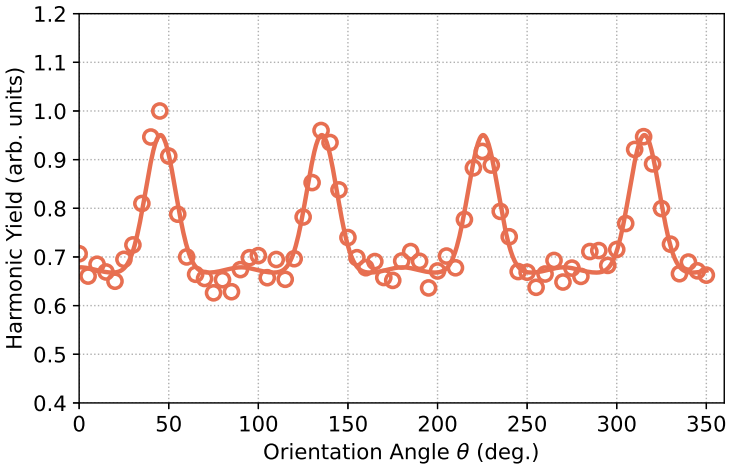

Figure S2: Orientation dependence of the third harmonic signal from MgO at an SWIR pump laser intensity of $2\,\mathrm{TW\,cm^{-2}}$ serving as a reference for the crystal angle calibration. Circles show experimental datapoints, solid line shows the numerical fit according to Eq. (1) of the main manuscript.

The deviation between datapoints and values of the fit function is calculated by

$$R^2(\theta) = (Y_{\mathrm{exp}}(\theta) - Y_{\mathrm{fit}}(\theta))^2 \tag{1}$$

where $Y_{\mathrm{exp}}(\theta)$ is the yield of a measured datapoint and $Y_{\mathrm{fit}}(\theta)$ is the value of the numerical fit function at a particular orientation angle θ. Figures S1(b), (e) and (h) show the $\theta-$dependent R^2 values for MgO, Al_2O_3 and LiF. For further analysis of the intensity-dependence of the fit quality, the R^2 values are integrated over the orientation angle θ and analyzed as a function of the SWIR pump laser intensity in Figs. S3(c), (f), and (i) for MgO, Al_2O_3 and LiF, respectively. The experimental data exhibit a significant level of agreement with the numerical fits, particularly concerning the high harmonic yields. However, it should be mentioned that a more noticeable deviation between the data and the fit is observed in the case of absorption. This discrepancy can be attributed to factors such as a lower signal-to-noise ratio and the less dynamic behavior of the measured transmission signal.

In order to analyze a potential harmonic order-dependent sensitivity of the signal strength

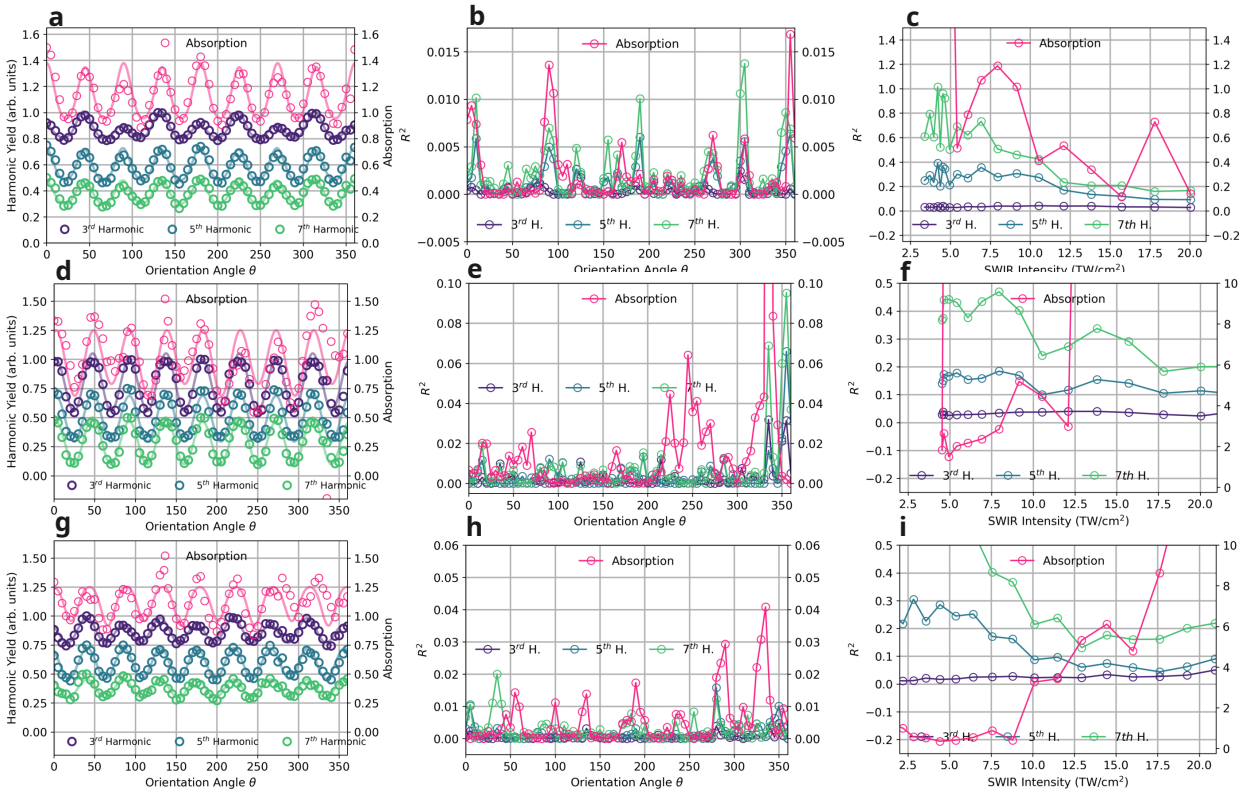

Figure S3: Representation of main experimental findings as Cartesian plots and analysis of the agreement between experimental datapoints and numerica fits. (a). θ-dependence of the observed odd harmonics and the SWIR absorption in a 200 µm thick MgO crystal obtained at a peak intensity of 18 TW cm^{-2}. Experimental datapoints are represented by circles, solid lines show the numerical fit according to Eq. (1). Curves are offset vertically for visibility. (b). R^2 analysis of the deviation between experimental data and the numerical fit function as a function of the orientation angle using Eq. 1. (c). Integrated R^2 over the orientation angle shown as a function of the SWIR pump laser intensity. (d) - (f). same as (a) - (c) for Al_2O_3. (g) - (i). same as (a) - (c) for LiF.

on the crystal orientation $dY/d\theta$ for the third, the fifth and the seventh harmonic in Fig. S4 using both the experimental data points (depicted by circles) and the numerical fits (solid lines). The amplitude of $dY/d\theta$ is significantly stronger for the fifth and the seventh harmonic when compared to the third harmonic for all three investigated materials. However, this amplitude is only reflected in A_{mono} and A_{dia} in Eq. (1) of the main manuscript. To further compare the width of the peaks we show the normalized harmonic yields of all observed harmonic orders as a function of the orientation angle in Figs. S4(c) for MgO, (f) for Al_2O_3 and (i)

for LiF. Here the yield of the third harmonic is added on a separate y-scale (see right y-axes, red circles) to artificially match the modulation amplitudes of the harmonics. The comparison shows that the maxima of all curves (see e.g. around 135°) exhibit roughly the same width which is consistent with the fact that we used $n = 3$ for the numerical fitting of all experimental data to reach an optimum agreement.

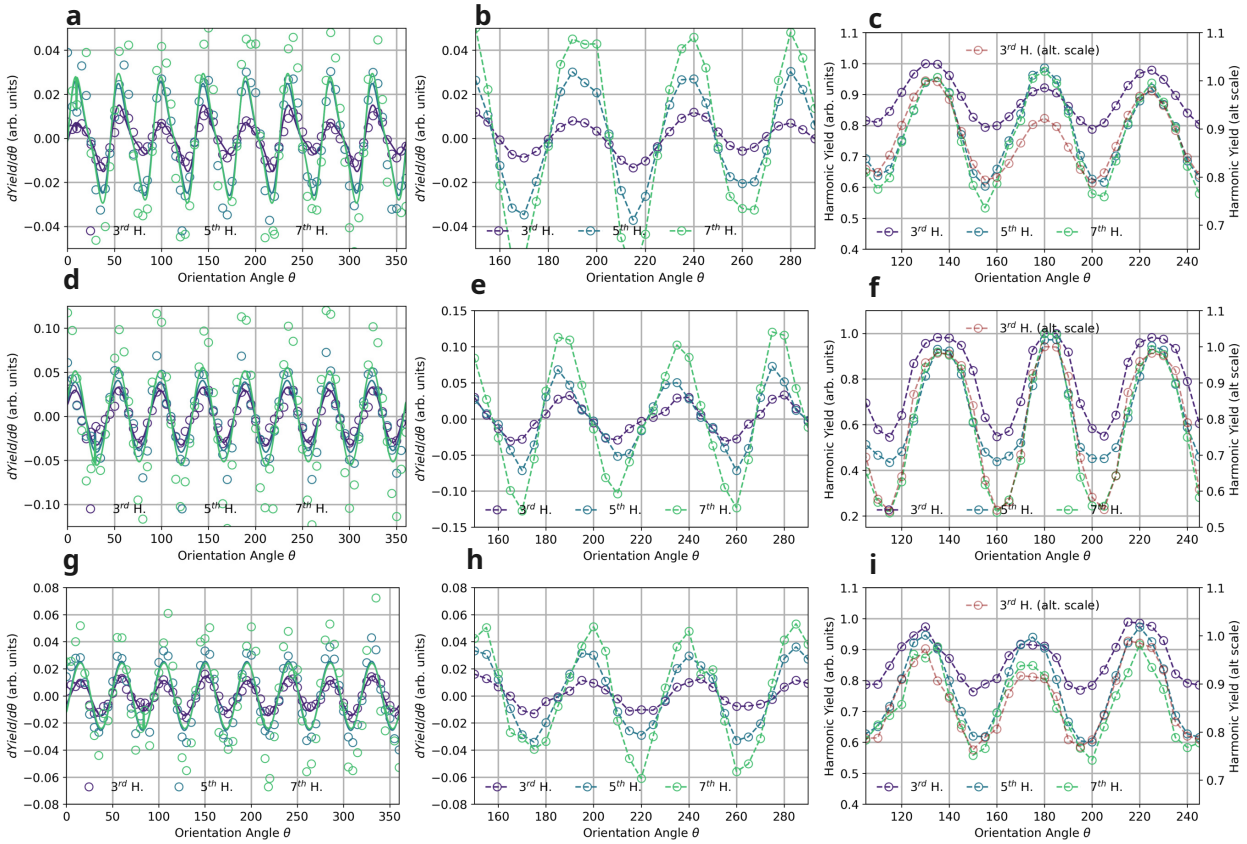

Figure S4: Numerical Analysis of the variation of the harmonic signal as a function of the orientation angle θ. (a). Derivative $dY/d\theta$ obtained from the numerical fits (solid lines) and from the experimental data (circles) in MgO as a function of the orientation angle. (b). Detailed view of the derivative $dY/d\theta$ only taking into account the experimental data. (c). Comparison of the width of $Y(\theta)$ on different scales of the y-axis to compare the relative width between different harmonic orders. (d) - (f). same as (a) - (c) for Al_2O_3. (g) - (i). same as (a) - (c) for LiF.

Orientation-Dependence of the SWIR Transmission

In Figs. 2(d), 3(c) and 4(c) of the main manuscript the mean transmission, averaged over all orientation angles is shown as a function of the SWIR peak intensity. Therein, the errorbars represent the standard deviation of the transmission values measured for the different orientation angles. In Fig. S5 we provide more detailed information on the intensity-dependent behavior of the transmission at characteristic angles in the used bulk crystals. Figure S5(a) compares the average transmission (as it is shown in Fig. 2(d) of the main manuscript) to the transmission at $\theta = 0°$, 25° and 45° representing the diatomic nearest-neighbour direction ($\theta = 0°$) the monoatomic nearest-neighbour direction ($\theta = 45°$ and at an inbetween angle ($\theta = 25°$. Especially at high SWIR intensities above $14\,\mathrm{TW\,cm^{-2}}$ the transmission along high symmetry directions (monoatomic and diatomic nearest-neighbour directions) is significantly lower compared the the intermediate case at $\theta = 25°$. This is due to the increased absorption at these orientation angles that is also apparent in Fig. S1. Similar results are observed for Al_2O_3 [see Fig. S5(b)] and for LiF (see Fig. S5(c)].

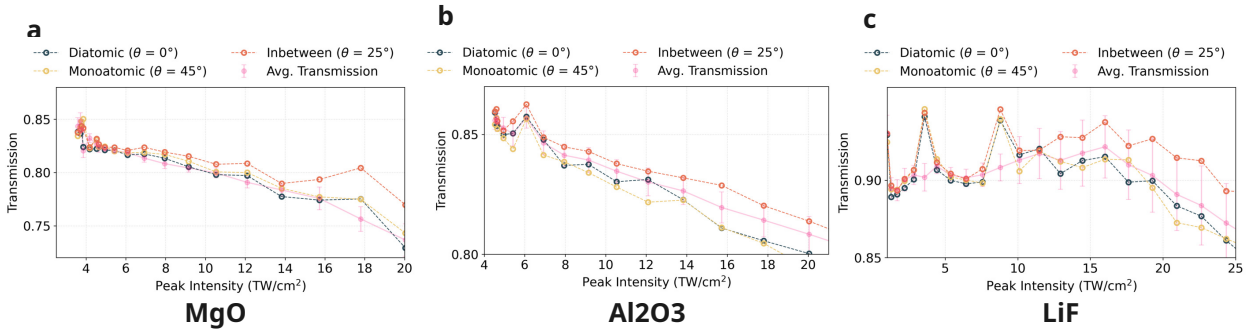

Figure S5: Comparison between the average intensity-dependent transmission to the transmission at specific crystal orientations. (a). Transmission results obtained in MgO. (b). Transmission results obtained in Al_2O_3. (c). Transmission results obtained in LiF.

XPW - Polarization Measurements

In the work presented in Ref.[2] the emergence of a cross-polarized wave (XPW) was held responsible for significant changes of the orientation dependence of the seventh harmonic

signal in GaAs. To investigate a potential influence of the XPW on our measurements we performed measurements on the polarization of the fundamental SWIR light before and after interaction with the bulk crystals. The results for MgO, Al_2O_3 and LiF as well as for amorphous SiO_2 are summarized in Fig. S6.

For two different intensities (one in the perturbative [Fig. S6(a)], one in the non-perturbative [Fig. S6(b)] regime) we measured the transmission through a linear polarizer as a function of the polarizer angle. Apart from a slight polarization rotation observed for Al_2O_3 at low intensity [see yellow circles in Fig. S6(a)] we do not observe any changes of the linear polarization state of the fundamental SWIR pulses. Hence we do not expect any influence of the XPW on the orientation-dependent measurements as were reported by P. Xia et al.

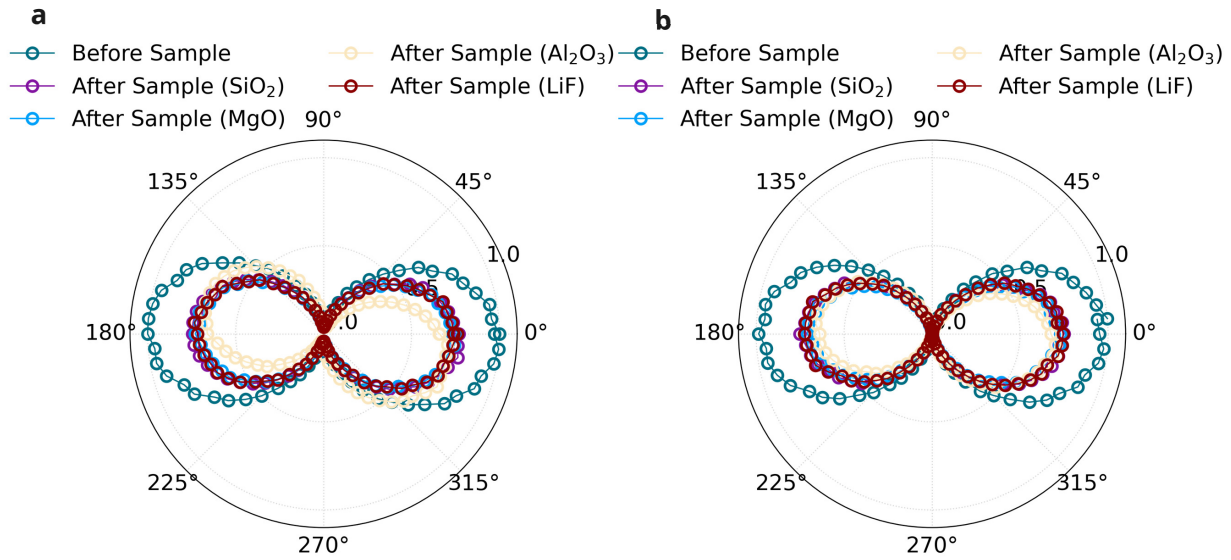

Figure S6: Experimental results to study the influence of a potential cross-polarized wave (XPW) on the orientation-dependence of the measured HHG signals. (a). shows the normalized transmission through a polarizer before the sample and after propagating through the used crystals as well as a 500 µm thick fused silica sample at a moderate SWIR intensity in the perturbative range. (b). Same as in (a) but at higher intensity in the non-perturbative regime.

Numerical Models

In this section we provide details on the numerical models that were used to obtain the results presented in Figs. (5) and (6) of the main manuscript. Afterwards we explain the reasoning behind choosing two different types of calculations, namely the semiconductor Bloch Equation calculations and the calculations of the photoionization rate using maximally-localized Wannier functions.

Semiconductor-Bloch Equations

We employed a semiconductor Bloch equations (SBE) model to simulate the generation of high harmonics from MgO. The SBE, as described in previous works,[3–5] was solved for a two-level system consisting of one valence band and one conduction band. Additionally, simulations for a three-level system involving one valence band and two conduction bands were conducted, but no significant differences were observed compared to the two-band system.

The advantage of using the semiconductor Bloch equations lies in its ability to directly determine the position of carriers in the momentum space (k-space) as a function of time. This feature provides a transparent and easily identifiable understanding of carrier dynamics.

In our study, we adopted a two-band length-gauge SBE approach to describe the dynamics of electrons and holes. This approach relies on the interband coherence polarization, denoted as p_k, and the electron (hole) occupation, denoted as $n_k^{e(h)}$. The governing equations for the SBE model are given as follows:

$$\begin{aligned} i\hbar\frac{\partial p_k}{\partial t} &= \left(\varepsilon_k^e + \varepsilon_k^h - i\frac{\hbar}{T_2}\right) p_k - (1 - n_k^e - n_k^h) d_k E(t) + ieE(t)\cdot\nabla_k p_k \\ \hbar\frac{\partial n_k^{e(h)}}{\partial t} &= -2\mathrm{Im}[d_k E(t) p_k^*] + eE(t)\cdot\nabla_k n_k^{e(h)} \end{aligned} \tag{2}$$

Here, $\varepsilon_k^{e(h)}$ represents the energies of the electrons in the conduction band and holes in the valence band, T_2 denotes the polarization dephasing time, d_k is the dipole transition matrix element, and $E(t)$ represents the electric field of the laser pulse.

The macroscopic polarization $P(t)$ and macroscopic current $J(t)$ are calculated by:

$$P(t) = \sum_k [d_k p_k + c.c.] \tag{3}$$

and

$$J(t) = \sum_{\lambda,k} v^\lambda(k) n_k^\lambda \tag{4}$$

with $\lambda \in \{h, e\}$ representing the valence and the conduction band and with the group velocity $v(k)$ given by:

$$v(k) = \nabla_k \varepsilon_k. \tag{5}$$

The harmonic spectral density at the sample plane is then defined as:

$$I_{\mathrm{HHG}}(\omega) = |\omega^2 P(\omega) + i\omega J(\omega)|^2 \tag{6}$$

The band structure of MgO (taken from Ref.[1]) that is used for the SBE calculations is visualized in Fig. S7 for crystal directions along $\Gamma - X$ and $\Gamma - K - X$.

Estimate of Wannier Jumping

Conventional computations of the angular dependence of the photoionization rate typically focus on carrier dynamics as described by vertical transitions in k-space. However, it should be noted that this approach, which holds true for many situations, does not consider non-vertical transitions in k-space and may neglect relevant contributions. Therefore here we aim to investigate the part of angular dependence of the photoionization rate which originates from direct transitions between states localized at different atoms. To this end, we developed a simple model for the photoionization rate based on the dipole moments between the

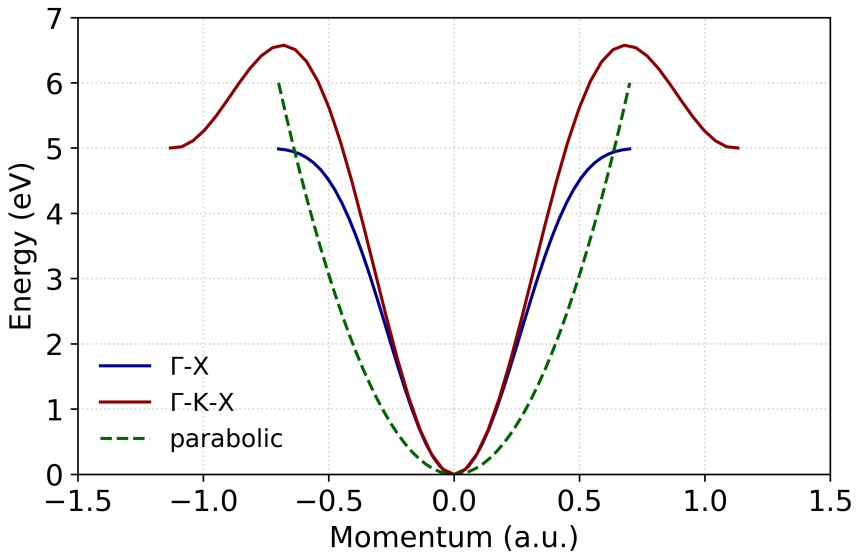

Figure S7: Band structure of MgO along the $\Gamma - X$ and $\Gamma - K - X$ direction used in the SBE calculations taken from Ref.[1]

localized (Wannier-basis) states.

The photoionization rate, which signifies the rate of transitions from the valence to the conduction band, was approximated using the multiphoton formalism:[6]

$$\Gamma \approx \sum_s |\vec{E} \cdot \vec{s}|^{2N(\vec{s})} d_s^{2N(\vec{s})} \tag{7}$$

Here the explicit dependence of the order of the nonlinear process on the orientation angle $N(\vec{s})$ is given by:

$$N(\vec{s}) = \frac{E_g - e\vec{E} \cdot \vec{s} r_s}{\hbar\omega}, \tag{8}$$

where $\vec{s}$ is the unit vector in the direction from an oxygen atom towards an atom indexed by s, E_g is the band gap, and r_s is the distance to the atom s. For the dipole momenta, we write

$$d_s = \int_V < \psi_O^g(\vec{r}) | (\vec{r} \cdot \vec{s}) | \psi_s^e(\vec{r} + \vec{s} r_s) > d\vec{r}, \tag{9}$$

where the transition from the oxygen atom ("O" subscript) is assumed, and ψ^g and ψ^e are

the localized wavefunctions which were approximated in atomic units by $A_s/\cosh(|\vec{r}|\sqrt{2I_p^{g,e}})$, where $I_p^{g,e}$ are the ionization potentials of the corresponding ground-state and excited-state atoms and A_s are the pre-factors corresponding to the distribution of the conduction-zone electrons: $A_O = 1$ and $A_{Mg} = 0.57$.

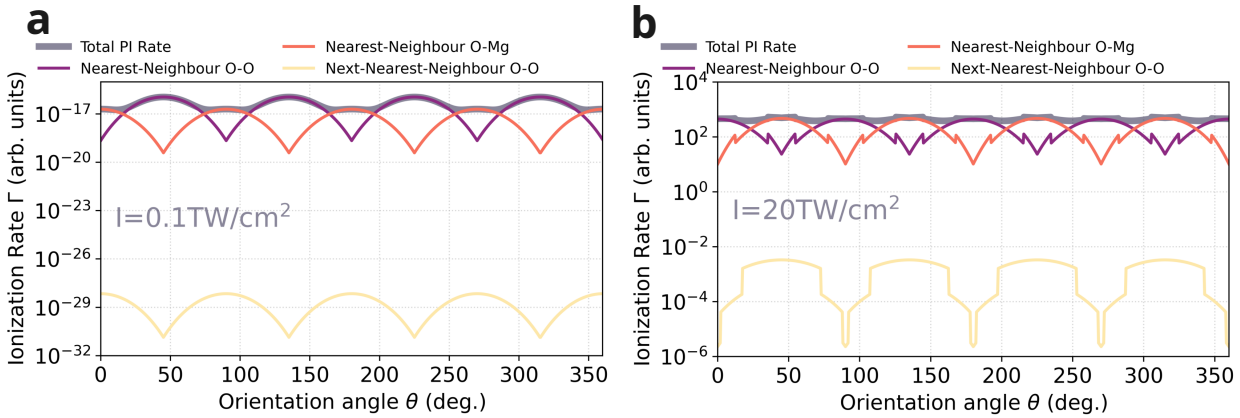

Figure S8: Angular dependence of the photoionization rate of the various nearest-neighbour and next-nearest-neighbour transitions calculated according to Eq. 7 at a SWIR peak intensity of (a). $0.1\,\mathrm{TW\,cm^{-2}}$ and (b). $20\,\mathrm{TW\,cm^{-2}}$.

Figure S8 shows the orientation dependence of the photoionization rates of the various nearest-neighbour and next-nearest-neighbour transitions computed by the Wannier-jumping formalism detailed above.

Since the localized part of the conduction band electron wavefunction resides mostly in the vicinity of the oxygen atoms[7] the transition moment of the O-Mg transition is significantly lower than that of the O-O transitions, which manifests itself in O-O transitions being preferred at lower intensities [see purple line in Fig. S8(a)]. As the intensity grows, the order of the multiphoton process n changes differently for the O-O transitions and for the O-Mg transitions due to different interatomic distances. This leads to the ionization rate for O-Mg transitions getting comparable to the ionization rate of O-O transitions [orange line in Fig. S8(b)]. Clearly, next-nearest neighbour transitions (see yellow line in Fig. S8(a)&(b) for the photoionization rate along O-Mg next-nearest-neighbour directions) are negligible under our experimental conditions.

Justification for Dual-Calculation Approach

In the main manuscript we show and discuss numerical results obtained from two different approaches, namely from the SBEs and from estimate of the photoionization rate based on dipole momenta between the localized states.

In MgO, the valence-band states are primarily localized at the oxygen atoms, while the conduction-band states exhibit a significant localization in the inter-atomic space as well as at the oxygen atoms.[7] Although the SBE calculations in principle have the capability to account for non-vertical transitions in momentum space between neighboring atoms when the corresponding dipole momenta are included, our specific implementation did not incorporate such indirect transitions. This limitation arises from the formalism and the specific construction of the dipole momenta employed in our calculations and caused us to augment the SBE results by estimates of angular dependence of the ionization rate due to jumping.

The SBE and Wannier-jumping calculations represent two different contributions to harmonic generation. In general, they are coupled and should be modelled simultaneously. However, in our case the fraction of carriers that are excited to the conduction band is low ($\leq 5\,\%$). Therefore, both processes are largely independent and decoupled, which validates our approach.

We would like to emphasize that photoionization processes are inherently included in the SBEs and are accurately reproduced when a sufficient number of bands is employed as a basis. However, incorporating photoionization phenomenologically into the SBEs, mirroring the approach taken in Eq. 2 of the main manuscript is unattainable due to the presence of a pre-factor in Eq. 2. Although this pre-factor can be theoretically derived, its practical implementation necessitates extensive fitting and adjustment to enable the seamless inclusion of Eq. 2 into the SBEs. Consequently, while Eq. 2 is well-suited for comparing interatomic transitions (Wannier-jumps) to other interatomic transitions. it does not facilitate a comparison between these interatomic transitions and the photoionization that is naturally included in the SBEs.

It is essential to emphasize that we fully acknowledge the complexities involved in interpreting the results obtained from SBE calculations, especially when attempting to extract specific information regarding the underlying mechanisms.

In summary, the utilization of both the SBE calculations and the photoionization rate estimates based on the dipole moments allows us to address different aspects of the HHG process in MgO, overcoming limitations inherent in each approach and providing a more comprehensive understanding of the phenomena under investigation.

Electron excursions associated with different intraband mechanisms

In the main manuscript it has been stated that the real-space excursion of carriers is comparable for both discussed intraband HHG mechanisms, namely the nonlinear current due to band anharmonicity and the injection current. In the case of the injection current, the excursion can be computed via the spatial coordinate of the tunneling exit x_0 [8]

$$x_0 = \frac{E_g}{q_e E} \tag{10}$$

where E_g is the bandgap, q_e the elementary charge and E denotes the electric field. In the case of the band anharmonicity the excursion of an conduction band electron that is accelerated by the laser field within a potential $\varepsilon(k)$ can be approximated from the SBE. Neglecting the population transfer and only considering the anharmonicity-related electronic motion in the conduction band the differential equation reads:

$$\frac{\partial p_k}{\partial t} = -\frac{i}{\hbar}\Delta\varepsilon(k)p_k \tag{11}$$

where $\Delta\varepsilon(k)$ denotes the deviation of the potential $\varepsilon(k)$ from a purely parabolic potential. Based on the analytic solution to Eq. 11

$$p_k(t) = \exp\{-i\Delta\varepsilon(k)t/\hbar\}p_k(0) \tag{12}$$

and the analytic expression for the conduction band given in Ref.[1] the real-space electron excursion x_{AH} due to band anharmonicity was approximated. For the third harmonic we obtain comparable values for the nonlinear current due to band anharmonicity and the injection current while for higher harmonic orders x_0 tends to reach larger values than x_{AH}. Thus, the injection current constitutes a serious candidate as an important intraband HHG mechanism.

Influence of nonlinear propagation effects

To estimate the influence of typical nonlinear propagation effects (e.g. self-phase modulation) on the obtained high-harmonic spectra and their orientation dependence we approximate the accumulated nonlinear phase (B-integral). Calculations based on the nonlinear refractive index of MgO of $3.9 \times 10^{-4}\,\mathrm{cm^2\,TW^{-1}}$ and a typical intensity of $10\,\mathrm{TW\,cm^{-2}}$ results in an accumulated phase of only $1 \times 2\pi$; the associated SPM-induced broadening of the spectrum will not have a significant effect on the propagation dynamics since the spectrum is initially comparatively narrow. The effect of GVD, characterized by $1.6\,\mathrm{fs^2}$ for MgO and the considered sample thickness, is very weak.

References

(1) You, Y. S.; Reis, D. A.; Ghimire, S. Anisotropic high-harmonic generation in bulk crystals. *Nature Physics* **2017**, *13*, 345–349.

(2) Xia, P.; Kim, C.; Lu, F.; Kanai, T.; Akiyama, H.; Itatani, J.; Ishii, N. Nonlinear prop-

agation effects in high harmonic generation in reflection and transmission from gallium arsenide. *Optics Express* **2018**, *26*, 29393–29400.

(3) Golde, D.; Meier, T.; Koch, S. W. High harmonics generated in semiconductor nanostructures by the coupled dynamics of optical inter-and intraband excitations. *Physical Review B* **2008**, *77*, 075330.

(4) Schubert, O.; Hohenleutner, M.; Langer, F.; Urbanek, B.; Lange, C.; Huttner, U.; Golde, D.; Meier, T.; Kira, M.; Koch, S. W.; others Sub-cycle control of terahertz high-harmonic generation by dynamical Bloch oscillations. *Nature Photonics* **2014**, *8*, 119–123.

(5) Lindberg, M.; Koch, S. W. Effective Bloch equations for semiconductors. *Physical Review B* **1988**, *38*, 3342.

(6) Ambrosek, D.; Oppel, M.; González, L.; May, V. Theory of ultrafast non-resonant multiphoton transitions: basics and application to CpMn (CO) 3. *Chemical Physics Letters* **2003**, *380*, 536–541.

(7) De Boer, P.; De Groot, R. The conduction bands of MgO, MgS and HfO_2. *Journal of Physics: Condensed Matter* **1998**, *10*, 10241.

(8) Jürgens, P.; Liewehr, B.; Kruse, B.; Peltz, C.; Engel, D.; Husakou, A.; Witting, T.; Ivanov, M.; Vrakking, M.; Fennel, T.; others Origin of strong-field-induced low-order harmonic generation in amorphous quartz. *Nature Physics* **2020**, *16*, 1035–1039.